CFD Simulation of a Transpiring-Wall SCWO Reactor: Formation and Optimization of the Water Film

Fengming Zhang
Guangdong Key Laboratory of Membrane Materials and Membrane Separation, Guangzhou Institutes of Advanced Technology, Chinese Academy of Sciences, 511458 Guangzhou, China

Shenzhen Institutes of Advanced Technology, Chinese Academy of Sciences, 518055 Shenzhen, China

Chunyuan Ma
National Engineering Laboratory for Coal-fired Pollutants Emission Reduction, Shandong University, 250061 Jinan, China

DOI 10.1002/aic.15021
Published online September 24, 2015 in Wiley Online Library (wileyonlinelibrary.com)

A two-dimensional axisymmetric computational fluid dynamics model of a transpiring wall reactor for supercritical water oxidation was developed using the commercial software Fluent 6.3. Numerical model was validated by comparisons with experimental temperature profiles and product properties (total organic carbon and CO). Compared with the transpiration intensity, the transpiring water temperature was found to have a more significant influence on the reaction zone. An assumption that an ideal corrosion and salt deposition inhibitive water film can be formed when the temperature of the inner surface of the porous tube is less than 374°C was made. It was observed that lowering transpiring water temperature is conducive to the formation of the water film at the expense of feed degradation. The appropriate mass flux ratio between the total transpiring flow and the core flow was determined at 0.05 based on the formation of the water film and feed degradation. © 2015 American Institute of Chemical Engineers *AIChE J*, 62: 195–206, 2016
Keywords: supercritical water oxidation, transpiring wall reactor, computational fluid dynamics, eddy, water film

Introduction

The thermophysical properties of supercritical water ($P_c = 22.1$ MPa, $T_c = 374$°C) are quite different from those at ambient conditions, and it is a good solvent for nonpolar organic compounds and gases such as oxygen, nitrogen, and carbon dioxide.[1,2] Supercritical water oxidation (SCWO) has been proven to be a promising technology to treat organic waste and recover energy.[3,4] Mass-transfer resistances are absent in a single-phase mixture of organic compounds and oxygen in supercritical water. It has been demonstrated that SCWO can destroy organic compounds with high efficiency (>99%), with a residence time of only a few seconds or within 1 min.[5–7]

However, two technical problems limit the commercial application of the SCWO technology over the past two decades.[8] First, supercritical water is a poor solvent for inorganic salts; thus, the plugging of the reactor, as well as the preheating and cooling section caused by the precipitation of sticky salts and solids can lead to a system shutdown.[9] Second, reactive ions can combine with high pressure, high temperature, excessive oxygen, leading to severe corrosion of the reactor, and other equipments.[10,11]

A transpiring wall reactor is a promising solution to solve both problems by fluid dynamics methods.[8,12,13] The transpiring wall reactor consists of a double shell reactor with an outer nonporous wall bearing high pressure and an inner porous wall.[14] Low-temperature (<400°C) transpiring water passes through the porous pipe to form a protective water film or at least a flushing effect on the surface.[15–22] Extensive experiments with the transpiring wall reactor has been made to reduce corrosion and avoid salt plugging.[8,12,13,23]

Getting insight into the detailed information of the reactor is very important for structural and operational optimization. However, the experimental results are usually limited to a small number of temperature measurements inside the reactor and effluent characterization due to the harsh environments inside the reactor.[24] Thus, the development of a computational fluid dynamics (CFD) technique is of great interest as it provides an alternative to obtain more information inside the reactor that is difficult to be measured.

CFD techniques have been applied by several authors to obtain detailed information in SCWO reactors. The CFD simulation of the SCWO process for a MODAR reactor was first developed by Oh et al.[25,26] Zhou et al. incorporated the SUPERTRAPP code for thermophysical properties of hydrocarbon mixtures.[27] Moussière et al. conducted a simulation using two reaction kinetics models, and the results showed that both models were in general agreement with the experimental data; the Eddy Dissipation Concept approach predicts more accurate temperature peak locations inside the reactor.[28]

Additional Supporting Information may be found in the online version of this article.

Correspondence concerning this article should be addressed to F. Zhang at zfmzhang8@163.com.

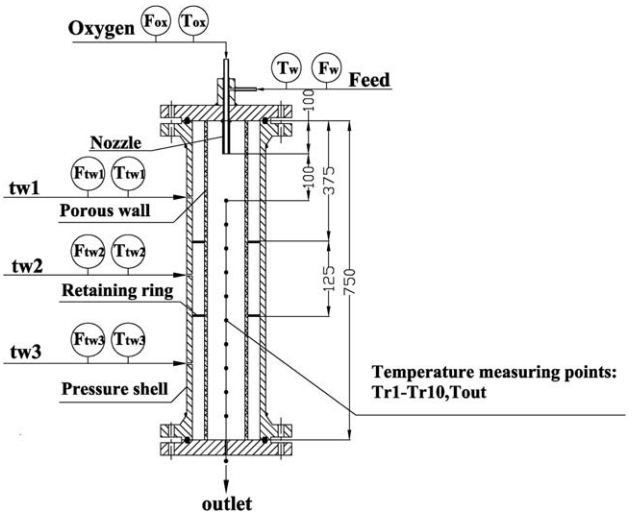

Figure 1. The schematic diagram of the transpiring wall reactor in Shandong University.

Q_w, Q_{ox}, Q_{tw1}, Q_{tw2}, and Q_{tw3} represent the mass flows of the feed, oxygen, the upper branch of transpiring water (tw1), the middle branch of transpiring water (tw2), and the lower branch of transpiring water tw3, respectively. T_w, T_{ox}, T_{tw1}, T_{tw2}, and T_{tw3} are the reactor inlet temperatures of the feed, oxygen, tw1, tw2, and tw3, respectively. Oxygen and tw3 are at room temperature.

However, the sensitiveness to the inlet temperature especially at subcritical temperature using Arrhenius law has been demonstrated.[28] It was observed that the reaction kinetics modeled by an Arrhenius law is suitable for describing SCWO process in transpiring wall reactor because the transpiring water was injected into reactor at subcritical temperature.[15,29,30]

CFD have been applied to obtain the velocity and temperature profiles inside the transpiring wall reactor. Abeln et al. carried out a steady-state calculation, and special attention was paid to the detailed information around the transpiring wall.[15] The effect of operating and structural parameters on the reactor's performance was investigated by Bermejo et al.[31] Hydrothermal flames are oxidation processes taking place in dense aqueous environments characterized by high temperatures and extremely fast reaction rates, and a transpiring wall reactor using a hydrothermal flame to avoid plugging in the preheating section was simulated by Lieball.[32] Their simulation results show that the velocity and temperature profiles are greatly dependent on their reactor structure and operating parameters. The formation of a corrosion and salt deposition inhibitive water film at a subcritical temperature on the inner surface of the porous wall is critical to the reactor's performance. However, no publication has focused on it.

In this study, a transpiring wall reactor was modeled by commercial CFD software (Fluent 6.3). A desalinated water-methanol mixture was used as artificial wastewater. Experimental data were provided to compare with simulation results. Special attention was paid to the temperature profiles near the inner surface of the porous tube that is hard to measure in the experiment. The effect of the key operating parameters such as transpiring water temperature and transpiration intensity on the formation of the water film and feed degradation was discussed for operating parameter optimization.

Experiment

Experimental setup

A schematic diagram of the transpiring wall reactor is presented in Figure 1. The inner porous tube of the transpiring wall reactor has a volume of approximately 1.8 L and a height of 750 mm. Detailed characteristic parameters of the porous tube can be seen in Table 1. A coaxial nozzle was used for the mixing of the feed and oxygen. The oxygen and the feed were injected into the reactor via the inner tube and the outer tube, respectively. Two retaining rings were used to separate the three transpiring zones. The reactor has been successfully operated in a pilot plant (feed flow: 8–17 kg h^{-1}, feed concentration: 2–8 wt %, transpiration intensity: 0.04–0.08, and transpiring water temperature: 200–350°C), and more details about the pilot plant and the transpiring wall reactor were given in previous works.[33,34]

It is possible to measure 10 different longitudinal temperatures with a 10-point K-type thermocouple (temperature range from 0 to 1000°C, accuracy: ±0.5%) installed at the center of the reactor. The exact points of the temperature measurements are shown in Figure 1.

Materials and analytical methods

Oxygen (purity > 99.9%) and deionized water (electric conductivity < 10 μS) were used as oxidant and transpiring water, respectively. Artificial wastewater was prepared with deionized water and methanol (purity > 99.9%). The TOC analysis of the aqueous effluent and the composition analysis of the gaseous effluent were performed with a TOC analyzer (Shimadzu, TOC 5000A) and a gas chromatograph (Agilent 6890 GC), respectively.

Model Description

Conservation equations and turbulence model

Considering that the multispecies flow, heat transfer, and reaction occur inside the transpiring wall reactor, the governing equations include continuity, momentum, energy, turbulence, and chemical species. Continuity equation is described by

$$\frac{\partial \rho}{\partial t} + \nabla \cdot (\rho \vec{u}) = 0 \tag{1}$$

where ρ and $\vec{u}$ are the fluid density and the velocity vector, respectively. Conservation of momentum is described by

$$\frac{\partial}{\partial t}(\rho \vec{u}) + \nabla \cdot (\rho \vec{u}\vec{u}) = -\nabla p + \nabla \cdot (\bar{\bar{\tau}}) + \rho \vec{g} + \vec{F} \tag{2}$$

where p is the static pressure, $\bar{\bar{\tau}}$ is the stress tensor, $\rho\vec{g}$ and $\vec{F}$ are the gravitational body force and the external body forces, respectively. $\vec{F}$ also contains other model-dependent source terms such as porous-media (as it will be show in "porous media"). The stress tensor $\bar{\bar{\tau}}$ is given by

Table 1. Characteristic Parameters of the Porous Tube

Material	Dimension (mm)	Porosity	Pore Size (μm)	Viscosity Coefficient (m^2)	Inertia Coefficient (m)
316L	Φ60 × 2.5	42.7%	20.8	6.2×10^{-12}	3.8×10^{-8}

$$\bar{\bar{\tau}}=\mu\left[\nabla\vec{u}+\nabla\vec{u}^{T}-\frac{2}{3}(\nabla\cdot\vec{u})I\right] \quad (3)$$

where μ is the molecular viscosity, I is the unit tensor, and the second term on the right-hand side of Eq. 3 is the effect of volume dilation.

We use an energy (E) balance to take into account the effect of heat transfer on hydrodynamics

$$\frac{\partial}{\partial t}(\rho E)+\nabla\cdot[\vec{u}(\rho E+p)]=\nabla\cdot\left[k_{\text{eff}}\cdot\nabla T-\sum_{j}h_j\vec{J}_j+(\bar{\bar{\tau}}_{\text{eff}}\cdot\vec{u})\right]+S_h \quad (4)$$

where k_{eff} is the effective conductivity, T is temperature, $\vec{J}_j$ is the diffusion flux of species j, and h_j is the specific enthalpy of species j. The first three terms on the right-hand side of Eq. 4 represent energy transfer due to conduction, species diffusion, and viscous dissipation. Sources of energy S_h due to chemical reaction is given by

$$S_h=-\sum_{i}\frac{h_i^0}{M_i}r_i \quad (5)$$

where h_i^0 is the enthalpy of formation of species i, M_i is molar mass of species i, and r_i is the volumetric rate of creation of species i. The species conservation is given by

$$\frac{\partial\rho Y_i}{\partial t}+\nabla\cdot\rho\vec{u}Y_i=-\nabla\cdot D_i\nabla Y_i+r_i,\ i=1,\ldots N_{\text{sp}} \quad (6)$$

where Y_i is the species mass fraction, D_i is mass diffusivity of species "i", r_i is the homogeneous species i production rate, and N_{sp} is the number of species. r_i is described by

$$r_i=\sum_{j}r_{ij} \quad (7)$$

where r_{ij} is the rate of production/consumption of species i in reaction j.

Previous studies[15,26,27] indicate that the RNG k-ε turbulence[35] model is more accurate to describe the flow recirculation and vortex shedding situations than the standard k-ε turbulence model. The RNG k-ε model was thus chosen as the turbulence model in the present study. The steady-state transport equations for k and ε in the RNG model are as follows

$$\frac{\partial}{\partial t}(\rho k)+\frac{\partial}{\partial x_i}(\rho k u_i)=\frac{\partial}{\partial x_j}\left(\alpha_k\mu_{\text{eff}}\frac{\partial k}{\partial x_j}\right)+G_k+G_b-\rho\varepsilon-Y_M+S_k \quad (8)$$

$$\frac{\partial}{\partial t}(\rho\varepsilon)+\frac{\partial}{\partial x_i}(\rho\varepsilon u_i)=\frac{\partial}{\partial x_j}\left(\alpha_\varepsilon\mu_{\text{eff}}\frac{\partial\varepsilon}{\partial x_j}\right)+C_1\frac{\varepsilon}{k}(G_k+C_3G_b)-C_2\rho\frac{\varepsilon^2}{k}-R_\varepsilon+S_\varepsilon \quad (9)$$

$$R_\varepsilon=\frac{C_\mu\eta^3(1-\eta/\eta_0)}{1+\beta\eta^3}\frac{\varepsilon^2}{k} \quad (10)$$

$$\eta=\frac{Sk}{\varepsilon} \quad (11)$$

where k and ε is the turbulent kinetic energy and the turbulent dissipation, respectively. G_k represents the generation of turbulence kinetic energy due to the mean velocity gradients, G_b is the generation of turbulence kinetic energy due to buoyancy, Y_M represents the contribution of the fluctuating dilatation in compressible turbulence to the overall dissipation rate, S_k and S_ε are user-defined source terms, S is the modulus of the rate of strain tensor, α_k and α_ε are the inverse effective Prandtl numbers for k and ε, respectively. $C_1=1.42$, $C_2=1.68$, $\eta_0=4.38$, $\beta=0.012$, $C_\mu=0.0845$, $\alpha_k=\alpha_\varepsilon=1.39$.

Kinetic model

For turbulence–chemistry interaction, the eddy dissipation model is in common use.[36] This model was developed for prediction of gaseous combustion reactions in turbulent flows. Considering that the transpiring water was injected into the reactor at subcritical temperature, the eddy dissipation model is not suitable for modeling the transpiring wall reactor, while a reaction kinetics based on Arrhenius law is more appropriate.[15,28–30] CO is the major intermediate of SCWO of methanol verified by previous experimental results[33] and other publications,[37–39] thus a two-step mechanism was adopted

$$CH_3OH+O_2=CO+2H_2O \quad (12)$$

$$CO+0.5O_2=CO_2 \quad (13)$$

The reaction rate is modeled by Arrhenius equation in Eqs. 14 and 15, and the reaction constants were obtained from literatures.[37,40] Given that oxygen was in large excess, its reaction order was assumed to be equal to zero

$$r_{CH_4O}=-\frac{d[CH_3OH]}{dt}=2.0\times10^{21}\times\exp\left(\frac{-326.6}{RT}\right)[CH_3OH] \quad (14)$$

$$r_{CO}=-\frac{d[CO]}{dt}=3.16\times10^{6}\times\exp\left(\frac{-112}{RT}\right)[CO] \quad (15)$$

Physical properties

The physical properties of water vary significantly near the critical point.[1] This severe spike can cause numerical instabilities when the energy equation is integrated. Hence, a suitable model for calculation of physical properties of the reaction mixture needs to be selected. The densities of pure species were calculated using the Peng–Robinson Equation[41] as shown in Eqs. 16–19, which was implemented using a Fluent User-Defined Function. Viscosities and thermal conductivities of the pure species were obtained from the NIST database.[42] The real heat capacity of water also peaks near the critical point that can lead to numerical instabilities. As such, an approximate curve was imported instead of the real heat capacity of water.[26,29] We assumed an ideal mixing for the mixture, and the physical properties of the mixture were computed based on mass fractions

$$P=\frac{RT}{(v-b_c)}-\frac{a_c\alpha}{v(v+b_c)+b_c(v-b_c)} \quad (16)$$

$$a_c=0.45724\frac{R^2{T_c}^2}{{P_c}^2};\ b_c=0.077796\frac{RT_c}{P_c} \quad (17)$$

$$\alpha=\left[1+\kappa(1-\sqrt{T_r})\right]^2 \quad (18)$$

$$\kappa=0.37464+1.54226\omega-0.26992\omega^2 \quad (19)$$

where v is the molar volume, a_c and b_c are EOS parameters, T_c is the critical temperature, P_c is the critical pressure, R is the universal gas constant, $T_r=T/T_c$ is the reduced temperature, κ is the constant characteristic of component, and ω is the acentric factor. More details about components physical properties can be found in Supporting Information Figures S1 and S2.

Porous media

Porous media were modeled by addition of a momentum source term to the standard fluid flow equations, and the source term consists of two parts: a viscous loss term and an inertial loss term

$$S_i = -\left(\frac{\mu}{\alpha}u_i + \frac{1}{2}\beta\rho|u|u_i\right) \tag{20}$$

where S_i is the source term for the ith momentum equation, $|u|$ is the magnitude of the velocity, α is the permeability. $1/\alpha$ and β correspond to viscous coefficient and inertial coefficient in Table 1, respectively. The supercritical water flowing through the porous wall follows Darcy's law.[18] Comparing with the operating pressure of the reactor (>22.1 MPa), the pressure drop across the porous wall can usually be neglected. Thus, no influence of pressure on the physical properties needs to be considered.

Fluent solves the standard energy transport equation in porous media regions with modifications to the conduction flux and the transient terms only. In the porous medium, the conduction flux uses an effective conductivity, and the transient term includes the thermal inertia of the solid region on the medium. The standard energy transport equation is given by

$$\begin{aligned}&\frac{\partial}{\partial t}[\chi\rho_f E_f + (1-\chi)\rho_s E_s] + \nabla\cdot[\vec{u}(\rho_f E_f + p)] \\ &= \nabla\cdot\left[k_{eff}\nabla T - \left(\sum_i h_i J_i\right) + \left(\bar{\bar{\tau}}\cdot\vec{u}\right)\right] + S_f^h\end{aligned} \tag{21}$$

where E_f is the total fluid energy, E_s is the total solid medium energy, χ is the porosity of the medium, k_{eff} is the effective thermal conductivity, and S_f^h is the fluid enthalpy source term.

The effective thermal conductivity in the porous medium, k_{eff} is computed as the volume average of the fluid conductivity (k_f) and the solid conductivity (k_s)

$$k_{eff} = \chi k_f + (1-\chi)k_s \tag{22}$$

As the transpiring water passes through the porous wall at subcritical temperature, multiphase effects may exist in a small area inside the reactor. Considering that our main objective is to obtain the temperature profiles near the porous wall, the existence of a two-phase flow inside the reactor has been neglected as a form of simplification.

Meshing and Numerical methodology

The two-dimensional axisymmetric geometry of the transpiring wall reactor was first represented in accordance to its actual size. The pressure-resistant vessel was not included in the computational domain and an assumption that transpiring water injecting form the inner surface of pressure shell was made. The mesh generation was performed with Gambit 2.2.30. Mesh was refined on the inner surface of the porous tube and the nozzle outlet, and a proper mesh size was determined by preliminary simulations (shown in Supporting Information Figures S3 and S4).

The reactor simulations are carried out by considering the following simplified boundary conditions: mass-flow-inlets were used to define oxygen, feed, and three branches of transpiring water. Pressure outlet boundary conditions are assigned to define the reactor outlet by eliminating the reverse flow problem. An axisymmetric boundary condition was used to define the reactor center. The porous tube was set as porous media zone.

In the simulations, the governing equations have been solved numerically with the code Fluent 6.3 using a finite volume numerical method. A segregated solver was selected. Pressure velocity coupling was achieved using the SIMPLE algorithm and second-order schemes were used. The steady-state simulation starts from an initial guess and the convergence criterion for velocity components, continuity and energy are 10^{-6}, 10^{-5}, and 10^{-8}, respectively.

Results and Discussion

Model validation

Transpiration intensity,[19] which is defined as the ratio between the mass flux of transpiring flows and the bulk, is an important parameter for reactor's performance

$$\varphi = \frac{(Q_{tw1}+Q_{tw2}+Q_{tw3})/(A_{tw1}+A_{tw2}+A_{tw3})}{(Q_w+Q_{ox})/A_b} \tag{23}$$

where A_b represents the inner circular area. A_{tw1}, A_{tw2}, and A_{tw3} represent the inner shell surfaces of the three transpiring zones, respectively. The same transpiring intensity for the three transpiring zones was set to in both the experiment and the simulation.

TOC removal efficiency (TOC_{rem}) is defined as the mass of total organic carbon eliminated divided by the total organic carbon introduced into the reactor

$$TOC_{rem} = \frac{Q_w TOC_{in} - (Q_w+Q_{tw1}+Q_{tw2}+Q_{tw3})TOC_{out}}{Q_w TOC_{in}} \tag{24}$$

where TOC_{in} and TOC_{out} symbolize the inlet and outlet concentration of TOC, respectively.

A comparison between experimental and calculated temperature profiles along the reactor axis at different feed concentrations is presented in Figure 2. Operating conditions in the simulation is $Q_w = 10$ kg h^{-1}, $T_w = 420$°C, $\varphi = 0.06$, $T_{tw1} =$ 360°C, $T_{tw2} = 200$°C, $\gamma = 2$, and the detailed experimental operating conditions are listed in Table 2. The oxidation reaction begins at the outlet of the nozzle, and the highest temperatures appear after a short development length. The reaction temperatures (50–100 mm below the nozzle outlet) are at 500–800°C in the experiment, which shows that the reaction is nearly conducted at the hydrothermal flame region.[24] Faster reaction rates in the upper section of the reaction are present in the experiments. The CFD model underpredicts the reaction temperatures, especially at high feed concentrations. In the middle part of the reactor, the error probably results from the simplification of the heat capacity of water and the neglect of the two-phase flow.[26,27] Despite this, relative errors between the experimental and calculated temperatures are less than 8%. At the lower part of the reactor, the calculated temperatures agree well with the measurements. Overall, the calculated temperature profiles were in agreement with the experimental data.

The outlet species concentrations in the simulation were also compared with the experimental ones. The products of incomplete oxidation of methanol can be characterized by TOC_{out}, TOC_{rem}, and CO in the gaseous effluent. The measurements of TOC_{out} and CO were usually conducted after a gas-liquid separator in the experiment. However, the gas-liquid separation process was neglected in the simulation. An assumption that the gas-liquid mixture from the reactor outlet has performed an ideal gas-liquid separation process in the

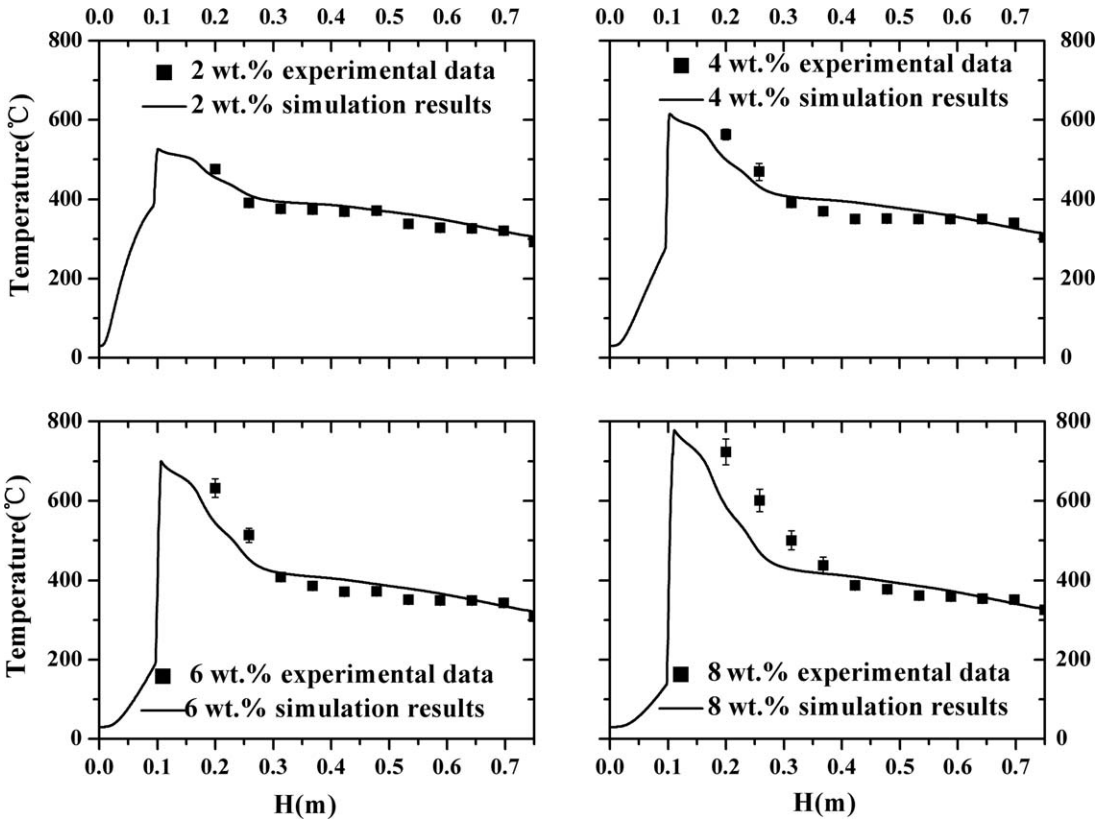

Figure 2. Comparisons of the experimental and the calculated temperature profiles along the reactor axis at different feed concentrations.

simulation was thus made to compare with the experimental data. Based on the simplification of the reaction kinetics of methanol, the gas-liquid mixture from the reactor outlet consists of CH_4O, O_2, CO, CO_2, and H_2O. After the assumed ideal gas-liquid separation process, the gaseous effluent in the simulation consists of O_2, CO, and CO_2, and the aqueous effluent consisted of CH_4O and H_2O.[43,44] TOC_{out} was only derived from the carbon of methanol in the aqueous effluent. Figure 3 shows comparisons of experimental and calculated TOC_{out}, TOC_{rem}, and CO, respectively. The trend and magnitude of TOC_{out}, TOC_{rem}, and CO in the simulation are in general agreement with experimental data, but a more significant trend is present in the simulation. We should remind that the outlet concentrations of TOC and CO are at trace level, and the quantities of TOC_{out} and CO is quite sensitive. The reaction is nearly conducted at the hydrothermal flame region at higher feed concentrations, and deviations between experimental results and numerical data are more significant at these conditions.

Similar conclusions can be obtained by comparisons of the experimental and calculated temperature profiles and effluent concentrations at different feed flows which are provided as Supporting Information Table S1, Figures S5 and S6.

Vector, temperature, and species concentration profiles

In this section, simulation results of the base case are discussed (Operating condition: $Q_w = 10$ kg h^{-1}, $C_w = 6$ wt %, $T_w = 420$°C, $\varphi = 0.06$, $T_{tw1} = 300$°C, $T_{tw2} = 200$°C, $\gamma = 2$). Figures 4a, b show calculated path lines colored by residence time. The residence time of fluid up to that point in the reactor can be characterized by color of lines. Figures 4c, d show vector of the reactor. Notably, eddies appear in the upper part of the reactor as shown in Figures 4b, d, which is mainly caused by jet entrainment of the feed stream.[18,45] Figures 4e, f show the temperature contour of the reactor. Higher temperature profiles are present near the porous tube in the upper part of the reactor. Although the eddy is favorable to enhancing reactants mixing and prolonging residence time, which is useful for the reaction and heat transfer, the reactive and hot fluid circulates and destroys the "water film" near the transpiring wall which is consistent with the previous studies.[18,28,29] Conversely, the hot reactive steams are cooled and diluted by transpiring water, which is not conducive for the reaction. A continuous stirred tank reactor is likely formed in the upper part of the reactor because of the strong mixing effect. The bulk flow and the transpiring water do not strongly mix in the

Table 2. Experimental Operation Conditions at Different Feed Concentrations

C_w[a] (wt %)	Q_w (kg h^{-1})	γ[b]	φ	T_w (°C)	T_{tw1} (°C)	T_{tw2} (°C)
2	9.9	2.21	0.060	418	358	205
4	10.1	1.92	0.061	420	357	200
6	9.9	2.14	0.058	421	361	197
8	9.9	2.30	0.058	417	358	204

[a]Feed concentration.
[b]Stoichiometric oxygen excess.

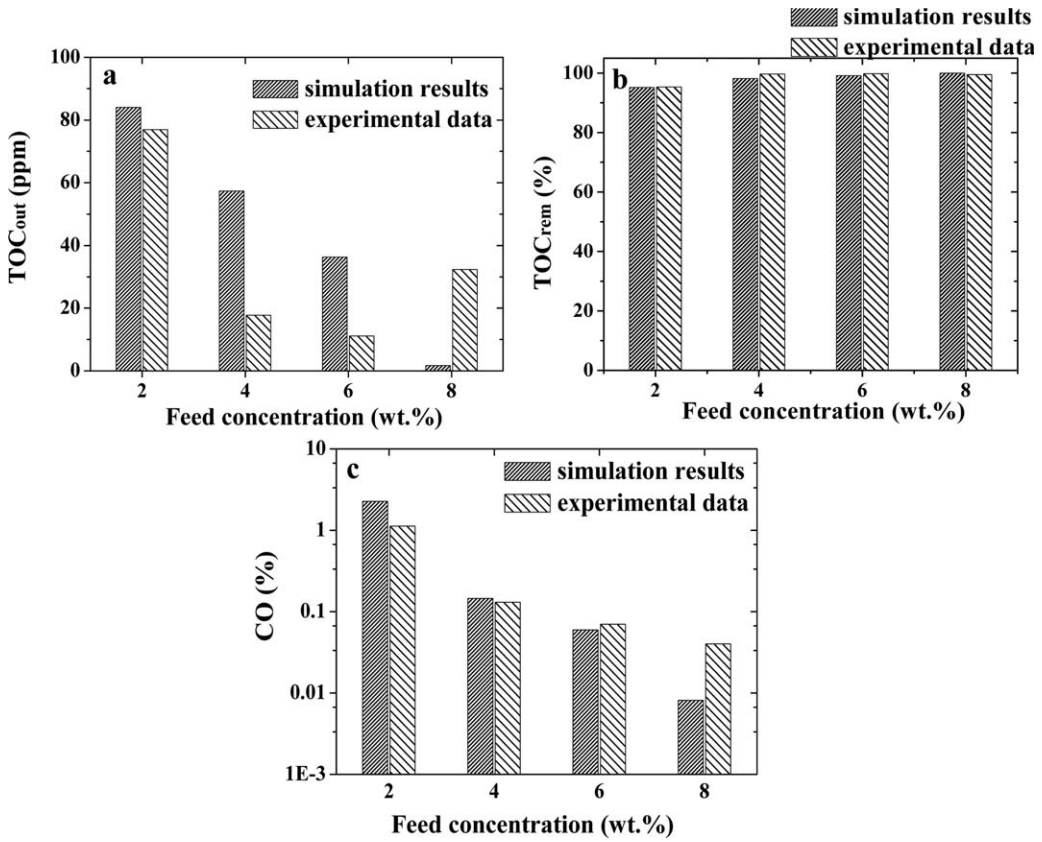

Figure 3. Comparisons of the experimental and calculated concentrations of the effluent at different feed concentrations: (a) TOC_{out}, (b) TOC_{rem}, (c) CO.

middle and lower part of the reactor, with a more uniform velocity forming. A plug flow reactor is formed in the middle and lower part of the reactor.

Species concentration contours are presented in Figure 5. The feed enters the reactor via the coaxial nozzle at supercritical conditions and reacts with oxygen. The methanol concentration rapidly decreases from 0.06 to 10^{-5} at 0–200 mm below the nozzle outlet. Thus, a fast oxidation reaction is present at the upper section of the reactor. Notably, mass concentrations of both methanol and CO in the porous tube and the annulus are about 10^{-5}. Reactants diffusing to the subcritical temperature area are not conducive to feed degradation for slower reaction rates. The quick decline of methanol at the nozzle outlet was also confirmed by the temperature contours

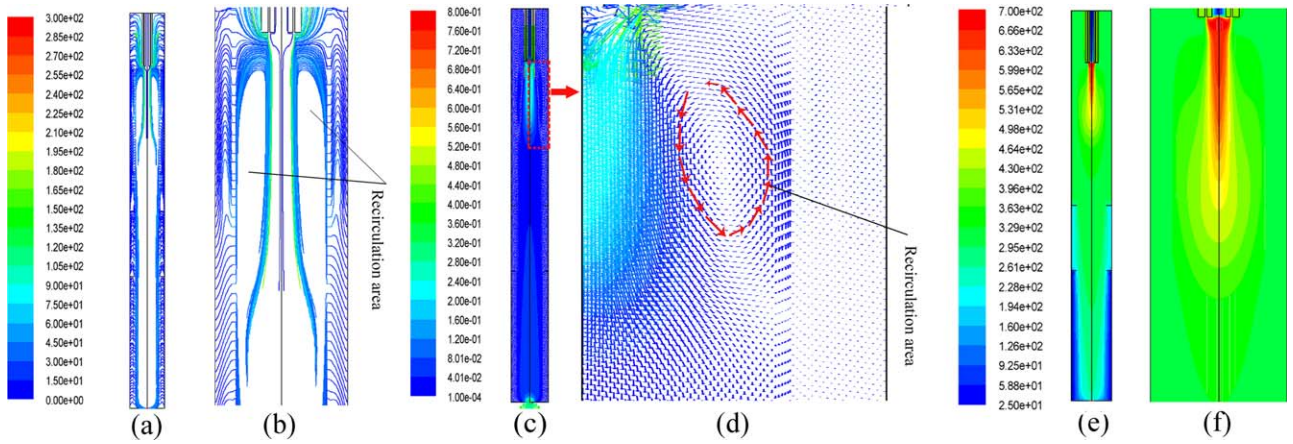

Figure 4. Calculated path lines, vector, and temperature contours of the reactor, (a) path lines colored by residence time (s) of the whole reactor, (b) an enlargement path lines (s) of the upper section of the reactor below the nozzle outlet, (c) vector (m s^{-1}) of the whole reactor, (d) an enlargement vector (m s^{-1}) of the upper part of the reactor below the nozzle outlet, (e) temperature contour (°C) of the whole reactor, (f) an enlargement temperature contour (°C) of the upper part of the reactor below the nozzle outlet.

[Color figure can be viewed in the online issue, which is available at wileyonlinelibrary.com.]

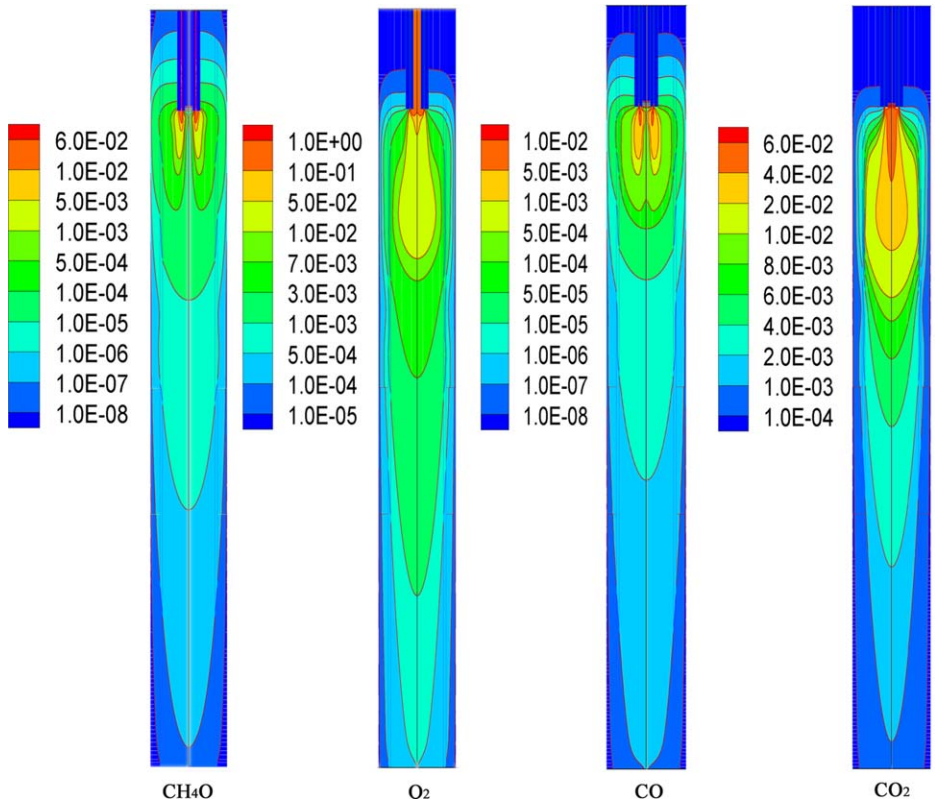

Figure 5. Calculated species contours inside the reactor.

[Color figure can be viewed in the online issue, which is available at wileyonlinelibrary.com.]

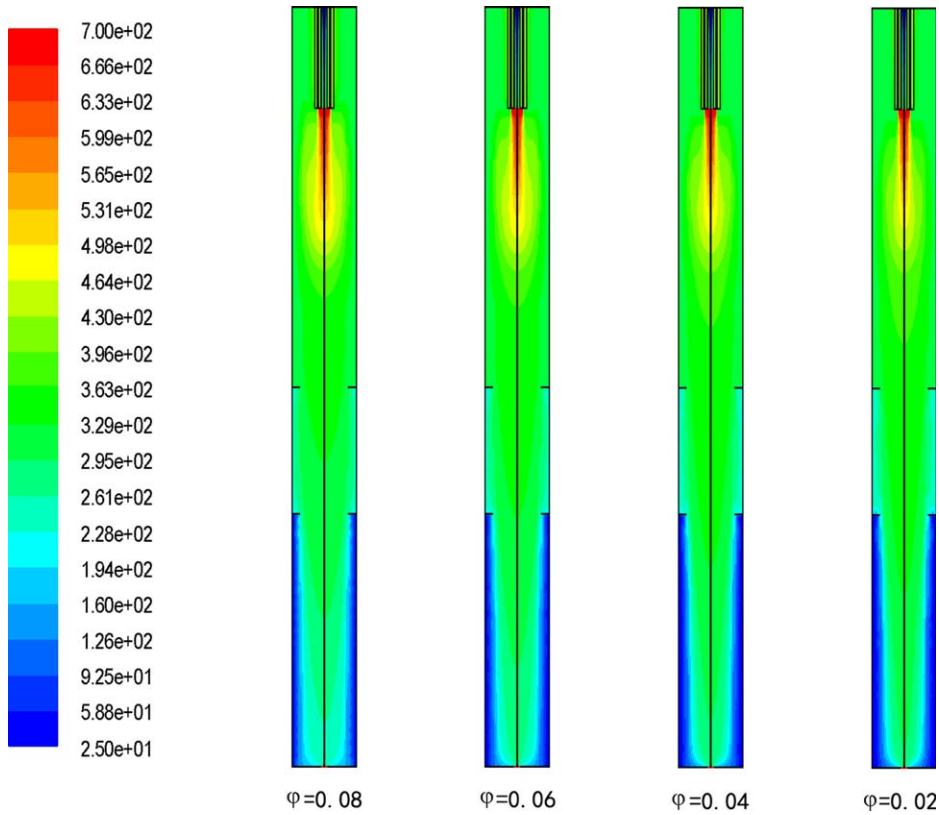

Figure 6. Calculated temperature contours (°C) of the reactor at different transpiration intensities.

Operating conditions in simulation: $C_w = 6$ wt %, $Q_w = 10$ kg h^{-1}, $T_w = 420$°C, $T_{tw1} = 360$°C, $T_{tw2} = 200$°C, $\gamma = 2$. [Color figure can be viewed in the online issue, which is available at wileyonlinelibrary.com.]

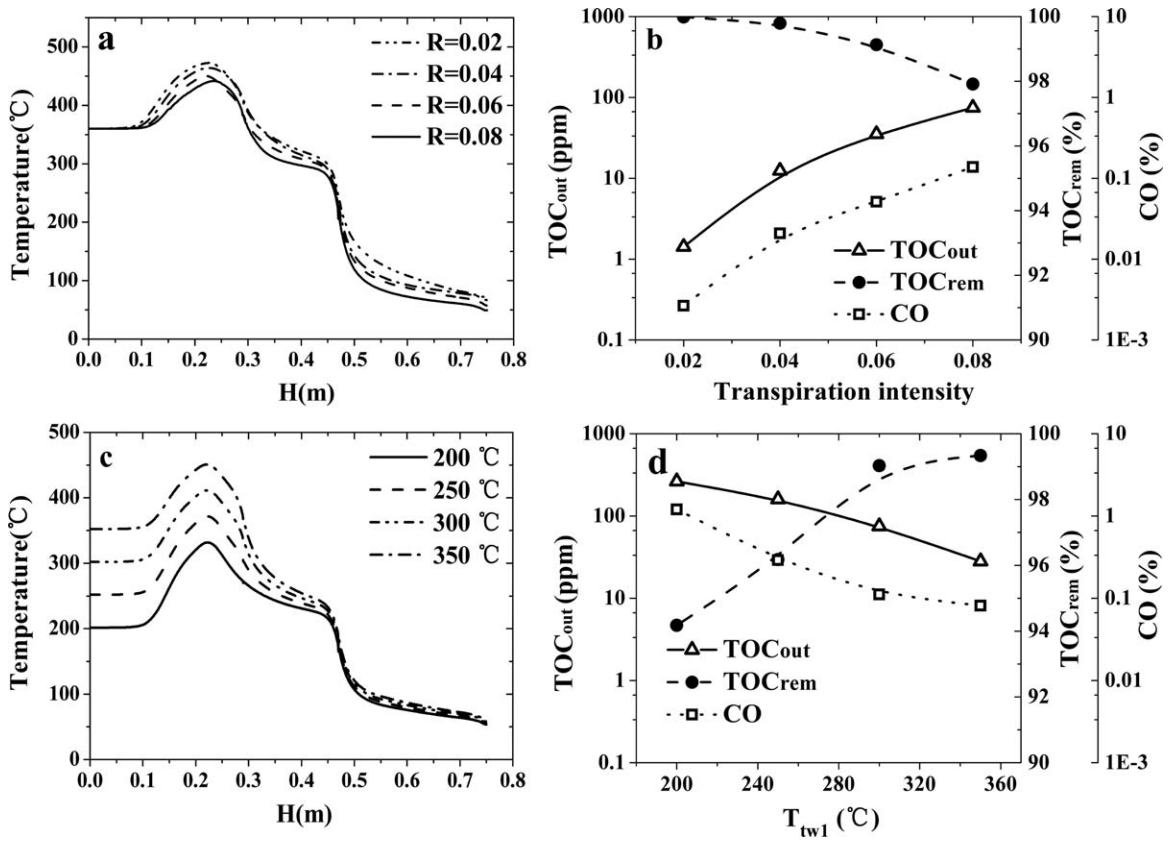

Figure 7. Effect of transpiration intensity and transpiring water temperature on the reactor's temperature profiles and product properties: (a) temperature profiles of the inner wall of the porous tube at different transpiration intensities, (b) product properties at different transpiration intensities, (c) temperature profiles of the inner wall of the porous tube at different transpiring water temperatures, (d) product properties at different transpiring water temperatures.

in Figures 4c, d. High temperature profiles at 0–100 mm below the nozzle indicate a flame-like burning. A radial temperature gradient was formed for the transpiring flow injection at subcritical temperature, and the bulk flow was cooled to subcritical temperature at the reactor outlet.

Transpiration intensity

The calculated temperature profiles at different transpiration intensities are plotted in Figure 6. The three branches of transpiring water were injected into the reactor at individual inlets with the same transpiration intensity, but at different temperatures (the temperature gradually declines from the top to the bottom). Simulation results show that the effect of transpiration intensity on the reaction zone is minimal. Lower temperature profiles are present in the middle and the lower section of the reactor at higher transpiration intensities because more transpiring water is injected at subcritical temperatures.

Higher transpiration intensities can provide higher radial velocities toward the central bulk flow and enhance the flushing effect on the inner surface of the porous tube. Figure 7a shows that lower temperatures at the inner surface of the porous tube are present at higher transpiration intensities. However, the temperature of the inner surface of the porous tube only decreases by 10°C when the transpiration intensity increases by 0.02. The effect of transpiration intensity on the temperature profiles of the inner surface of the porous tube is thus not significant. The overall residence time at supercritical temperature decreases because of the increase of transpiring flows.[33] Figure 7b shows that a gradual increment trend of both the TOC_{out} and CO is present with the increase of transpiration intensity, which is consistent with our previous experimental data.[33] TOC_{out}, TOC_{rem}, and CO are 1.4 ppm, 99.99%, and 0.003% at a transpiration intensity of 0.02, respectively. When the transpiration intensity is increased to 0.08, TOC_{out} and CO increase to 74.9 ppm and 0.139%, respectively, and TOC_{rem} is depressed to 97.82%.

Transpiring water temperature

Considering that the reaction zone is mainly located in the upper section of the reactor, the discussion of the effect of transpiring water temperature only focuses on the temperature of tw1. Figure 8 shows that the temperature profiles in the reactor are greatly dependent on the temperature of tw1. Higher reaction temperatures are present at higher transpiring water temperatures. This condition indicates that the temperature of tw1 has a direct impact on the reaction zone. The lower temperature profiles are also present in the middle and the lower part of the reactor at lower transpiring water temperatures.

Figure 7c shows the effect of tw1 on the temperature profiles of the inner surface of the porous tube. The temperatures of the inner surface of the porous tube significantly decrease when T_{tw1} was decreased. However, Figure 7d shows that TOC_{out} and CO greatly increase when tw1 is decreased. TOC_{rem} increases accordingly from 96.16 to 99.81% when the transpiring water

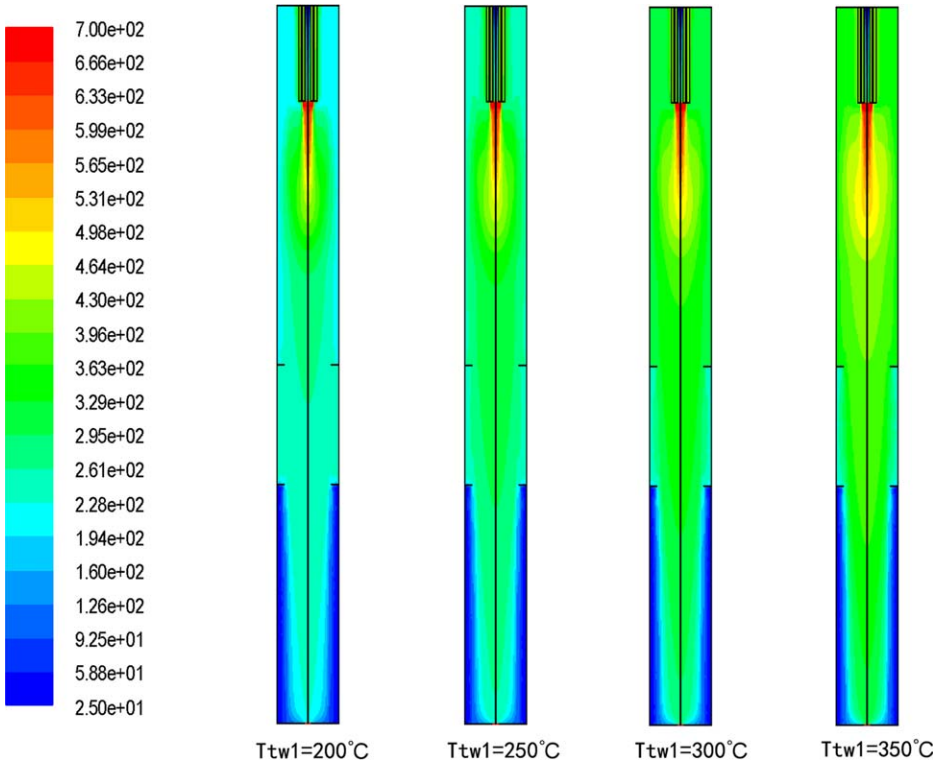

Figure 8. Calculated temperature contours (°C) of the reactor at different transpiring water temperatures.

Operating conditions in simulation: $C_w = 6\%$, $Q_w = 10$ kg h^{-1}, $\varphi = 0.06$, $T_w = 420$°C, $T_{tw2} = 200$°C, $\gamma = 2$. [Color figure can be viewed in the online issue, which is available at wileyonlinelibrary.com.]

temperature is increased from 200 to 350°C. Hence, the transpiring water temperature can be minimized on the premise of high oxidation efficiency of the feed for energy saving.

Moreover, the effect of feed flow on the temperature profiles and product properties was provided as Supporting Information Figures S7 and S8, and the results show

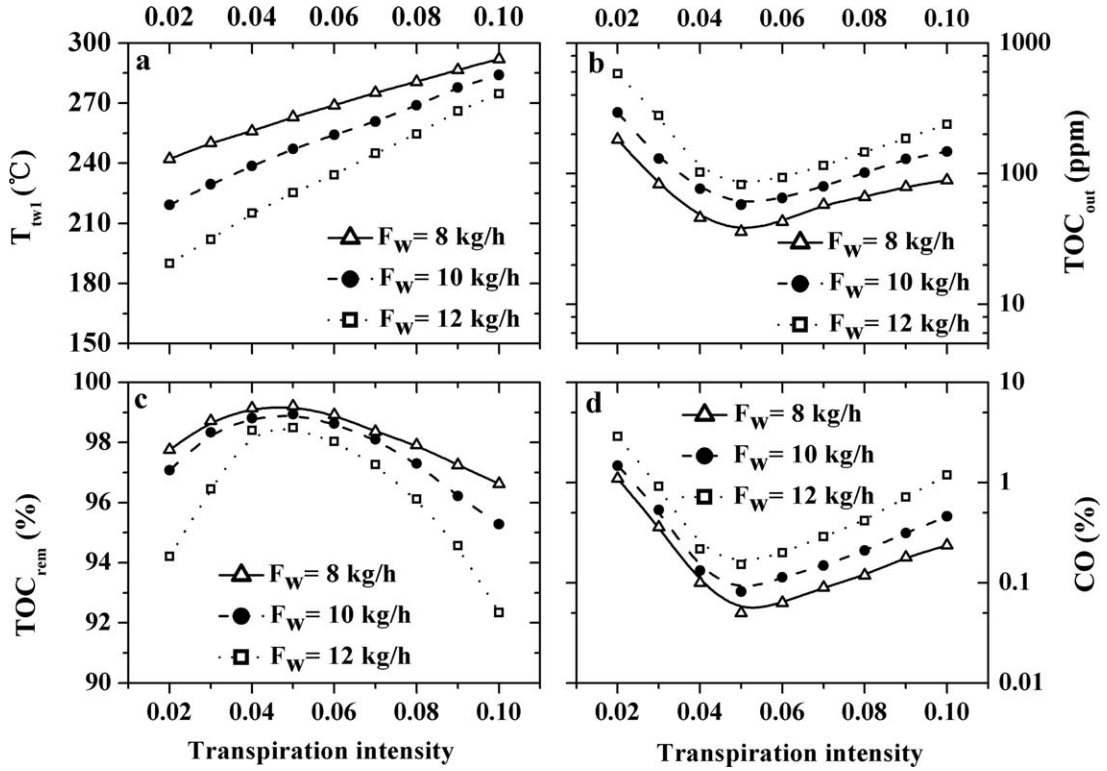

Figure 9. Characteristics of (a) water film formation temperature ($T_{tw1,cr}$), (b) TOC_{out}, (c) TOC_{rem}, (d) CO as functions of transpiration intensity for different feed flow rates.

that the effect of feed flow on water film formation is not significant.

Optimization of the water film

The transpiring wall reactor's anticorrosion performance and avoidance of salt plugging is usually dependent on the formation of a water film at a subcritical temperature on the inner surface of the porous wall. However, it cannot be measured or displayed by experiment or simulation. When the temperature of the inner surface of the porous tube exceeds 374°C, the transpiring water can only flush the inner wall surface without dissolving inorganic salts. The formation of the ideal water film is thus dependent on the temperatures of the inner surface of the porous tube. In this article, an assumption that the ideal water film can be formed when the temperature of the inner surface of the porous tube is less than 374°C was made. We define water film formation temperature ($T_{tw1,cr}$) as the highest temperature of tw1 to keep the water film present, and thus obtaining $T_{tw1,cr}$ is an interesting and attractive point.

Figure 9a shows the $T_{tw1,cr}$ as functions of the transpiration intensity for different feed flow rates (operating condition: $Q_w = 8$–12 kg h^{-1}, $C_w = 6$ wt %, $T_w = 420$°C, $\varphi = 0.02$–0.10, $T_{tw2} = 200$°C, $\gamma = 2$). Higher values for $T_{tw1,cr}$ are present at higher transpiration intensities. The $T_{tw1,cr}$ increases from 219.2 to 284.1°C when the transpiration intensity is increased from 0.02 to 0.10 at a feed flow rate of 10 kg h^{-1}. Lower values of the $T_{tw1,cr}$ appear at higher feed flow rates. The $T_{tw1,cr}$ decreases from 242.2 to 190.1°C when the feed flow rate increases from 8 to 12 kg h^{-1} at a transpiration intensity of 0.02.

The oxidation reaction of the feed is suppressed when the temperatures of the inner surface of the porous tube are kept at less than 374°C. Figures 9b–d show the aqueous and gaseous effluent as functions of transpiration intensity for different feed flow rates. TOC_{out} and CO present a "V" as a function of transpiration intensity. The minima of TOC_{out} and CO are seen to be present at a transpiration intensity of 0.05. TOC_{rem} also presents a reverse "V" as a function of transpiration intensity. It can be seen that the maxima of TOC_{rem} is also present at transpiration of 0.05. Although TOC_{out} and CO will increase with the increase of the transpiration intensity at the same T_{tw1}, the lower values of $T_{tw1,cr}$ appear at lower transpiration intensities. This condition greatly increases TOC_{out} and CO. The increase of the feed flow rate will also shorten the useful residence time, resulting in lower oxidation efficiencies.

Lower transpiration intensities and lower $T_{tw1,cr}$ should be adopted to keep the water film present on the inner surface of the porous tube for energy saving. The proper transpiration intensity for the reactor is determined at 0.05, taking into account a higher oxidation efficiency of methanol.

Conclusion

A numerical model of a transpiring wall reactor for SCWO was presented. Numerical model was validated by comparisons with experimental temperature profiles, aqueous, and gaseous products. It was found that the model presents some inaccuracies in the temperature profiles of the transcritical zone, which is attributed to the simplification in the heat capacity of water and the neglect of the two-phase flow. The effect of the key operating parameters on flow fields of the reactor especially the temperature near the porous tube was analyzed.

The presence of the recirculation areas caused by jet entrainment is an important feature of the flow field inside the reactor. The transpiration intensity has small influence on the reaction zone, while the transpiring water temperature has a direct impact on both the reaction temperature and the reactor effluent. It is observed that lower transpiring water temperatures are conducive to the formation of the water film, at the expense of feed degradation efficiency. The appropriate transpiration intensity for the reactor was determined at 0.05 based on the formation of the water film and feed degradation.

Acknowledgment

This work is supported by National High Technology Research and Development Program (No. 2007AA05Z235), Guangdong-Hongkong Breakthrough Bidding Project in Key Areas (No. 2012A090200001), Research Project of High Tech Industry in Nansha District (No. 2013P013), PhD Start-Up Fund of Natural Science Foundation of Guangdong Province (No. 2014A030310203), Guangdong Province Science and Technology Plan Project (No. 2013B091100003), Shenzhen Basic Research Project (No. JCYJ20150316144639927).

Notation

Abbreviations

A = area, m^2
A_b = inner circular area, m^2
a_c = coefficient in Peng–Robinson equation
b_c = coefficient in Peng–Robinson equation
C = concentration, wt %
C_P = specific heat, J kg^{-1} K^{-1}
D = mass diffusivity, m^2 s^{-1}
E = energy, J
E_f = total fluid energy, J
E_s = total solid medium energy, J
F = external body forces, N
g = acceleration due to gravity, 9.8 kg s^{-2}
G_b = generation of turbulence kinetic energy due to buoyancy
G_k = generation of turbulence kinetic energy due to the mean velocity gradients
h_i^0 = species i
h_j = specific enthalpy of species j
I = unit tensor
k = turbulent kinetic energy
J = diffusion flux, kg m^{-2} s^{-1}
k_{eff} = effective thermal conductivity in the porous medium, W m^{-1} k^{-1}
k_f = thermal conductivity for the fluid phase, W m^{-1} k^{-1}
k_s = thermal conductivity for the solid medium, W m^{-1} k^{-1}
M = molar mass, kg mol^{-1}
N_{sp} = number of species
P = pressure, Pa
Q = mass flow rate, kg h^{-1}
r = reaction rate
R = universal gas constant, 8.3145 kJ mol^{-1}
S = modulus of the rate of strain tensor
S_f^h = rm
S_h = sources of energy due to chemical reaction
S_i = ith the source term for porous media momentum equation
S_k, S_ε = user-defined source terms
t = time, s
T = temperature, °C
T_r = reduced temperature
$T_{tw1,cr}$ = water film formation temperature, °C
TOC = total organic carbon, ppm
u = velocity vector, m s^{-1}
v = molar volume, m^3 mol^{-1}
x = direction in space
Y = species mass fraction

Y_M = contribution of the fluctuating dilatation in compressible turbulence to the overall dissipation rate

Greek letters

α = permeability, m^2
α_k = inverse effective Prandtl numbers for k, $\alpha_k = 1.39$
α_ε = inverse effective Prandtl numbers for ε, $\alpha_\varepsilon = 1.39$.
β = inertial resistance factor, m
γ = stoichiometric oxygen excess
κ = constant characteristic of component
ε = turbulent dissipation
μ = molecular viscosity, Pa s
ρ = fluid density, kg m^{-3}
τ = stress tensor, N
φ = transpiring intensity
χ = porosity of the medium
ω = acentric factor

Subscripts

tw1 = upper branch of transpiring water
tw2 = middle branch of transpiring water
tw3 = lower branch of transpiring water tw3
ox = oxygen
w = feed
c = critical

Literature Cited

1. Akiya N, Savage PE. Roles of water for chemical reactions in high-temperature water. *Chem Rev*. 2002;102:2725–2750.
2. Gao LA, Liu YD, Wen LY, Huang WX, Mu XH, Zong BN, Fan HL, Han BX. The effect of supercritical water on the hydroconversion of Tahe residue. *AIChE J*. 2010;56:3236–3242.
3. Vadillo V, Belén García-Jarana MB, Sánchez-Oneto J, Portela JR, de la Ossa EJM. Simulation of real wastewater supercritical water oxidation at high concentration on a pilot plant scale. *Ind Eng Chem Res*. 2011;50:2512–2520.
4. Bermejo MD, Cocero MJ, Fernandez-Polanco F. A process for generating power from the oxidation of coal in supercritical water. *Fuel*. 2004;83:195–204.
5. Vielcazals S, Mercadier J, Marias F, Mateos D, Bottreau M, Cansell F, Marraud C. Modeling and simulation of hydrothermal oxidation of organic compounds. *AIChE J*. 2006;52:818–825.
6. Sugiyama M, Tagawa S, Ohmura H, Koda S. Supercritical water oxidation of a carbon particle by Schlieren photography. *AIChE J*. 2004;50:2082–2089.
7. Bermejo MD, Rincon D, Martin A, Cocero MJ. Experimental performance and modeling of a new cooled-wall reactor for the supercritical water oxidation. *Ind Eng Chem Res*. 2009;48:6262–6272.
8. Vadillo V, Sánchez-Oneto J, Portela JR, de la Ossa EJM. Problems in supercritical water oxidation process and proposed solutions. *Ind Eng Chem Res*. 2013;52:7617–7629.
9. Hodes M, Marrone PA, Hong GT, Smith KA, Tester JW. Salt precipitation and scale control in supercritical water oxidation–part A: fundamentals and research. *J Supercrit Fluids*. 2004;29:265–288.
10. Kritzer P. Corrosion in high-temperature and supercritical water and aqueous solutions: a review. *J Supercrit Fluids*. 2004;29:1–29.
11. Kritzer P, Boukis N, Dinjus E. Review of the corrosion of nickel-based alloys and stainless steels in strongly oxidizing pressurized high-temperature solutions at subcritical and supercritical temperatures. *Corrosion*. 2000;56:1093–1104.
12. Bermejo MD, Cocero MJ. Supercritical water oxidation: a technical review. *AIChE J*. 2006;52:3933–3951.
13. Chen Z, Wang GW, Mirza ZA, Yang S, Xu YJ. Study of transpiring fluid dynamics in supercritical water oxidation using a transparent reactor. *J Supercrit Fluids*. 2014;88:117–125.
14. Daman EL. *Process and Apparatus for Supercritical Oxidation*. U.S. Patent 5,571,423. November 5, 1996.
15. Abeln J, Kluth M, Böttcher M, Sengpiel W. Supercritical water oxidation (SCWO) using a transpiring wall reactor: CFD simulations and experimental results of ethanol oxidation. *Environ Eng Sci*. 2004;21:93–99.
16. Bermejo MD, Fdez-Polanco F, Cocero MJ. Experimental study of the operational parameters of a transpiring wall reactor for supercritical water oxidation. *J Supercrit Fluids*. 2006;39:70–79.
17. Crooker PJ, Ahluwalia KS, Fan Z, Prince J. Operating results from supercritical water oxidation plants. *Ind Eng Chem Res*. 2000;39:4865–4870.
18. Fauvel E, Joussot-Dubien C, Tanneur V, Moussière S, Guichardon P, Charbit G, Charbit F. A porous reactor for supercritical water oxidation: experimental results on salty compounds and corrosive solvents oxidation. *Ind Eng Chem Res*. 2005;44:8968–8971.
19. Wellig B, Lieball K, Rudolf Von Rohr P. Operating characteristics of a transpiring-wall SCWO reactor with a hydrothermal flame as internal heat source. *J Supercrit Fluids*. 2005;34:35–50.
20. Xu DH, Wang SZ, Tang XY, Gong YM, Guo Y, Wang YZ, Zhang J. Design of the first pilot scale plant of China for supercritical water oxidation of sewage sludge. *Chem Eng Res Des*. 2012;90:288–297.
21. Zhang FM, Xu CY, Zhang Y, Chen SY, Chen G, Ma CY. Experimental study on the operating characteristics of an inner preheating transpiring wall reactor for supercritical water oxidation: temperature profiles and product properties. *Energy*. 2014;66:577–587.
22. Gong WJ, Duan XJ. Degradation of landfill leachate using transpiring-wall supercritical water oxidation (SCWO) reactor. *Waste Manag*. 2010;30:2103–2107.
23. Zhang FM, Chen SY, Xu CY, Chen GF, Ma CY. Research progress of supercritical water oxidation based on transpiring wall reactor. *Chem Ind Eng Prog*. 2011;30:1643–1650.
24. Augustine C, Tester JW. Hydrothermal flames: from phenomenological experimental demonstrations to quantitative understanding. *J Supercrit Fluids*. 2009;47:415–430.
25. Oh CH, Kochan RJ, Charlton TR, Bourhis AL. Thermal-hydraulic modeling of supercritical water oxidation of ethanol. *Energy Fuel*. 1996;10:326–332.
26. Oh CH, Kochan RJ, Beller JM. Numerical analysis and data comparison of a supercritical water oxidation reactor. *AIChE J*. 1997;43:1627–1636.
27. Zhou N, Krishnan A, Vogel F, Peters WA. A computational model for supercritical water oxidation of organic toxic wastes. *Adv Environ Res*. 2000;4:75–90.
28. Moussière S, Joussot-Dubien C, Guichardon P, Boutin O, Turc HA, Roubaud A, Fournel B. Modelling of heat transfer and hydrodynamic with two kinetics approaches during supercritical water oxidation process. *J Supercrit Fluids*. 2007;43:324–332.
29. Leybros A, Roubaud A, Guichardon P, Boutin O. Supercritical water oxidation of ion exchange resins in a stirred reactor: numerical modelling. *Chem Eng Sci*. 2012;69:170–180.
30. Narayanan C, Frouzakis C, Boulouchos K, Prikopsky K, Wellig B, Rudolf von Rohr P. Numerical modeling of a supercritical water oxidation reactor containing a hydrothermal flame. *J Supercrit Fluids*. 2008;46:149–155.
31. Bermejo MD, Martín Á, Queiroz JPS, Bielsa I, Ríos V, Cocero MJ. Computational fluid dynamics simulation of a transpiring wall reactor for supercritical water oxidation. *Chem Eng J*. 2010;158:431–440.
32. Lieball K. *Numerical Investigations on a Transpiring Wall Reactor for Supercritical Water Oxidation*. PhD Thesis. Switzerland: ETH Zurich, 2003.
33. Zhang FM, Chen SY, Xu CY, Chen GF, Zhang JM, Ma CY. Experimental study on the effects of operating parameters on the performance of a transpiring-wall supercritical water oxidation reactor. *Desalination*. 2012;294:60–66.
34. Zhang FM, Chen SY, Xu CY, Chen GF, Ma CY. Energy consumption analysis of a transpiring-wall supercritical water oxidation pilot plant based on energy recovery. *Desalination Water Treat*. 2013;51:7341–7352.
35. Orszag SA, Yakhot V, Flannery WS, Boysan F, Choudhury D, Maruzewski J, Patel B. *Near-Wall Turbulent Flows*. New York: Elsevier Science Publishers, 1993.
36. Magnussen BF. On the structure of turbulence and a generalized eddy dissipation concept for chemical reaction in turbulent flow. In: *Proceedings of the 19th American Institute of Aeronautics and Astronautics Aerospace Science Meeting*. St. Louis, January 1981:12–15.
37. Li L, Chen P, Gloyna EF. Generalized kinetic model for wet oxidation of organic compounds. *AIChE J*. 1991;37:1687–1697.
38. Tester JW, Webley PA, Holgate HR. Revised global kinetic measurements of methanol oxidation in supercritical water. *Ind Eng Chem Res*. 1993;32:236–239.

39. Vogel F, Blanchard JLD, Marrone PA, Rice SF, Webley PA, Peters WA, Smith KA, Tester JW. Critical review of kinetic data for the oxidation of methanol in supercritical water. *J Supercrit Fluids*. 2005;34:249–286.
40. Dagaut P, Cathonnet M, Boettner J. Chemical kinetic modeling of the supercritical-water oxidation of methanol. *J Supercrit Fluids*. 1996;98:33–42.
41. Wilding WV, Rowley RL. A four-parameter corresponding-states method for the prediction of thermodynamic properties of polar and nonpolar fluids. *Int J Thermophys*. 1986;7:525–539.
42. Thermophysical Properties of Fluid Systems. NIST. 2012. Available at http://webbook.nist.gov/chemistry/fluid/.
43. Baranenko VI, Fal'kovskii LN, Kirov VS, Kurnyk LN, Musienko AN, Piontkovskii AI. Solubility of oxygen and carbon dioxide in water. *Atom Energy*. 1990;68:342–346.
44. Emerson S, Stump C, Wilbur D, Quay P. Accurate measurement of O_2, N_2, and Ar gases in water and the solubility of N_2. *Mar Chem*. 1999;64:337–347.
45. Queiroz JPS, Bermejo MD, Cocero MJ. Numerical study of the influence of geometrical and operational parameters in the behavior of a hydrothermal flame in vessel reactors. *Chem Eng Sci*. 2014;112:47–55.

Manuscript received Dec. 15, 2014, and revision received Aug. 19, 2015.